

Supporting Information

Scheffer et al. 10.1073/pnas.1108268108

SI Methods

Isolation and freezing of chicken erythrocyte nuclei. Chicken erythrocyte nuclei were isolated from a chicken erythrocyte suspension (Charles River Laboratories) essentially as previously described (1, 2). Erythrocytes were pelleted by centrifugation at $800 \times g$ and suspended in 20-fold excess of ice-cold wash buffer (5 mM Hepes, pH 7.5, 150 mM NaCl, 0.5 mM phenylmethylsulphonyl fluoride) and pelleted again at $800 \times g$. To maintain chromatin compaction the subsequent steps were carried out in magnesium-containing lysis buffer (MLB) (15 mM Hepes, pH 7.5, 2 mM $MgCl_2$, 60 mM KCl, 15 mM NaCl, 0.1 mM phenylmethylsulphonyl fluoride) (1). For lysis of the cytoplasmic membrane, erythrocytes were resuspended in MLB containing 0.5% Nonidet P-40. The resuspension was then incubated at room temperature for 5 min. Nuclei were collected at 1,000 g and washed twice in MLB containing 0.1% Nonidet P-40. Then nuclei were pelleted again and resuspended in 50-fold excess of 15 mM Hepes NaOH containing 20 mM NaCl, 0.1 mM phenylmethylsulphonyl fluoride, and 20% dextran (40 kDa, Sigma-Aldrich). Colloidal gold particles of 10 nm in diameter, equilibrated with the same buffer, were added to the nuclei as fiducials, then nuclei were pelleted at 5,000 g for 15 min. Pellets were transferred into flat 3-mm copper carriers with a 0.1 mm indentation (Engineering Office M. Wohlwend GmbH) and cryofixed using the HPM010 high-pressure freezer (Boeckeler Instruments). In our preliminary studies we also used aluminum carriers for freezing and the appearance of the fibers was identical, thus we conclude that the material of the carrier did not affect our observations. Because aluminum carriers are not as suitable for sectioning, all of the subsequent sectioning was performed with copper carriers. We also minimized the amount of contact time (never exceeded 20 sec) of the sample with the carrier before freezing to reduce any potential influence of the carrier material on the sample.

Cryosectioning. The carriers containing frozen nuclei pellets were transferred to the cryochamber of a Leica EM FC6/UC6 ultramicrotome at $-140^\circ C$ and mounted into the flat chuck of the microtome. A part of the contour wall of the carrier was removed to expose the sample. A pyramid block was prepared in an arbitrary region of the sample using a 20° diamond trimming knife (Diatome). Thin cryosections were obtained with a 35° diamond knife (Diatome) at $-140^\circ C$ with a cutting speed of 0.4 mm s^{-1} , and the nominal sectioning feed set to 50 nm for 2D overview images and to 80–100 nm for tomography. Section ribbons were collected on the knife edge by an eyelash mounted to a wooden stick, and then carried to the central area of the carbon side of a C-flat grid (Protochips) and attached using an electrostatic charging device (Haug). Grids with sections were moved to grid storage boxes (Gatan) and stored in liquid nitrogen. Electron diffraction was used to verify the vitreous state of water in the cryosections.

Tilt-Series Collection. Well-vitrified sections with minimal cutting distortions were selected for tomography acquisition. We collected 52 single-axis tilt-series. The tilt-series typically covered an angular range from -60° to $+66^\circ$ and were collected with a 1.5° angular increment on a Tecnai G2 Polara 300 kV microscope (FEI), cooled to liquid nitrogen temperature, and equipped with a Gatan post column GIF 2002 energy filter set to 30 eV slit width. Data acquisition was carried out under low-dose conditions using the UCSF tomography software (3). Images were re-

corded on a $2k \times 2k$ pixel CCD camera at a defocus level between $-8 \mu\text{m}$ and $-6.5 \mu\text{m}$ at a magnification of $22,500\times$ where the pixel size at the specimen level is 0.6 nm. The total electron dose was around $90 \text{ e}^-/\text{\AA}^2$ per tilt-series. Tilt-series were aligned using the fiducialless alignment software Alignator (4).

Tomographic Reconstruction. Tomographic reconstructions were calculated by weighted back projection with a Fourier filter at the first zero crossing. CTF correction was not considered because the resolution of our subtomogram average was far within the first zero crossing of the CTF (resolution approximately 4.3 nm and the first zero crossing is approximately 3.4 nm), and thus CTF correction would not provide any additional information. The merit figure of the aligned series used for the reconstructions and subsequent processing was approximately 1 nm for all datasets (Table S1).

Fiber Detection. The tomograms were mildly low-pass filtered to suppress high-frequency noise. Fibers were detected in the tomograms using a template-matching approach with a filtered binary cylinder with a length of 60 nm and a diameter of 30 nm (5). Several putative fibers were detected, the longest of which was approximately 240 nm long, which was lying in the plane of the section. This approach is often implemented in real space reconstruction of helical polymers, in which a solid cylinder is used as an initial reference in multireference alignment of 2D images of filaments (6). From the positions of the highest cross-correlation, subtomograms were automatically extracted. The minimum allowed distance between two selected subtomograms was greater than 20 nm. The procedure as applied on three tomographic reconstructions is presented in the flowchart diagram in Fig. S6.

Due to inherent limitations of the template matching approach we classified the subtomograms using principal components analysis (7) and KerDenSom3D (8), in order to remove false positive fibers, as well as fibers selected with an incorrect fiber-axis orientation. For this a spherical mask with diameter of 60 nm was used. Strict selection of the class averages was performed, using stringent criteria, which excluded subtomograms with crevasses or knife marks, subtomograms containing fibers with their fiber axes misaligned, or fibers which were bent or too tightly packed.

Subtomogram Averaging and Classification of 30-nm Fibers. Approximately 1,000 subtomograms remained for the subsequent subtomogram averaging. Classification of the subtomograms did not show any obvious misorientations anymore but rather showed structural differences within the fibers. All subtomograms were visually inspected and no obvious misalignments or false selections could be found.

The subtomogram alignment and averaging processes are guided by the directive to avoid any template bias. We used subtomograms masked with a cylinder of diameter 38 nm and a length of 60 nm to align all subtomograms with respect to a filtered binary cylinder. The alignment was restricted only by the fact that the fibers were not allowed to rotate more than 30° degrees from their originally estimated fiber axis determined by template matching. In this way, we guaranteed that no top views could misalign to side views. The missing wedge was taken into account in all alignment and averaging steps. The final average showed density along the entire length of the 60 nm (Fig. S2). We again checked the correct alignment of the fiber axes (that no side views were incorporated with top views) by PCA classification. The averaging converged to show a subtomogram average depict-

ing a checkerboard pattern from the side view. Because the helical order in the final subtomogram average was evidently short-range, we shortened the mask for alignment to 40 nm. By restricting the angular scan to 30 degrees from the originally estimated fiber axis, we were certain that no misalignment could occur, even though a shorter mask was applied for the alignment. All other parameters (i.e., the two remaining Euler angles and all translations) remained free during the process.

The subtomogram averaging with the smaller mask converged to a structure with a similar checkerboard pattern as before, only that the densities were significantly better resolved. The resulting resolution was estimated to be approximately 4.3 nm, according to the 0.5 FSC criterion. The reproducibility of the final subtomogram average was verified on three separate datasets from different tomograms. The fiber retained its elongated shape >60 nm in length and always showed the same diameter of approximately 32 nm. The region outside the mask remained dense with less clear structures because they were not used for the averaging process. Lastly, we classified the aligned subtomograms. For this we used PCA (7) and KerDenSOM3D (8), both missing-wedge compensated. We varied the size of the masks and analyzed the modifications of the structure.

Addressing Compression Artifacts. It has recently been shown by Pierson et. al (9) that small robust structures within a larger volume are able to resist section-induced compression. The 30-nm fibers in chicken erythrocyte nuclei did not suffer largely from compression artifacts, as judged by the cross sections of individual fibers (Fig. 1*A* and *B*). Even so, any potential directional distortion that might exist would be compensated for by the isotropic distribution of Euler angles (Fig. S3), although this might contribute to a resolution loss, due to an artificial increase in flexibility in the nucleosome densities. The subtomogram is circular when computationally projected down the fiber axis evidencing that no directional distortion is present.

H1/H5 and Histone Tail Modeling. By hydroxyl radical mapping studies and molecular modeling as well as conventional EM of isolated chromatin it is known that H1/H5 binds to the entry–exit point of the linker DNA. We have simulated data using a partitioned tetranucleosome (10) providing a mononucleosome with linker DNA, with the molecular model of H5 positioned at the entry–exit pseudodyad axis of the DNA, to provide the DNA stem structure seen in typical EM studies (11). We can certainly say by the location of the linker histone (periphery of the fiber interior) and by virtue of its small size that it cannot account for the densities in the fiber cavity. This also applies to the histone core tails. Only approximately 12 amino acids of the H4 tail, for example, extend beyond the nucleosome core, resulting in a span of approximately 2 nm—which is far less than required for creating density in the center of the fiber. A single DNA linker has three times higher molecular mass (approximately 33 kDa per 55 bp) than all expanded histone tails (two H3 tails and two H4 tails: 2×30 residues + 2×12 residues = ~ 9 kDa), which can in principal reach the fiber interior.

FSC Calculation. Aligned subtomograms were divided into odd and even numbers and two separate half-dataset averages were cre-

ated. The Fourier shell correlation was computed over 32 shells and the resolution was determined by the 0.5 cutoff criterion.

Symmetry Determination. We did not impose symmetry during the iterative alignment procedure, as is the case with iterative helical real space reconstruction in alignment of 2D filaments (6), which requires an initial search estimate. In this manner, presumption of helical symmetry is completely avoided. Firstly, to find the symmetry parameters, we calculated the autocorrelation functions of the subtomogram average in cylindrical coordinates. This was performed in Matlab (The Mathworks) using custom scripts based on the algorithm as described below. In cylindrical coordinates $\rho(r, \phi, z)$ the 3D density distribution of the subtomogram average is unfolded in circular shells (ϕ is the rotation around the fiber axis) of different radii r , where z is the translation along the fiber axis. Thus, the auto-correlation peaks may be considered as the lattice points of a helical net, which may be indexed by direction vectors (Fig. 3*B*). When an object is helical, the density repeats itself after applying an azimuthal rotation of $\Delta\phi$, and an axial translation of Δz . We thus describe our fiber in terms of these parameters.

Symmetry Imposition. Because the positions of the nucleosomes clearly showed a helical pattern, we symmetrized the 30-nm fiber in order to generate an idealized fiber. Helical reconstruction, in the traditional sense, was not required because this process reconstructs a 3D object from a 2D image. In our case, we have the true 3D density, from which the symmetrization parameters can be directly derived. Thus after calculating the position of the nucleosomes and deriving the symmetrization parameters (axial translation Δz 3.4 nm and azimuthal rotation $\Delta\phi = 54^\circ$), according to the visible lattice points of the cylindrical autocorrelation function as depicted by the red spheres in Fig. 3*A* and *B*, the subtomogram average ρ was subjected to the following transformations in Cartesian space:

- i. For the 6 nucleosomes of the first gyre—i.e., $n = -2, -1, -1, 1, 2, 3$ — $\rho n(r, \phi + n\Delta\phi, z + n\Delta z)$ was calculated, and for 7 nucleosomes in the second gyre $k = -3, -2, -1, 0, 1, 2, 3$ $\rho k(r, \phi + k\Delta\phi + 54^\circ * 203^\circ, z + k\Delta z + 1.7 \text{ nm})$.
- ii. The final symmetrized density was the summation of ρn and ρk for $n = -2, -1, -1, 1, 2, 3$ and $k = -3, -2, -1, 0, 1, 2, 3$. Because no missing information was present in the subtomogram average, compensation in Fourier space was not necessary.

Alignment of Subtomograms Against a Mononucleosome Template.

Dense positions with the approximate volume of a single nucleosome were automatically detected using the watershed algorithm (12). Subtomograms were extracted around these points and were aligned against a mononucleosome template. The template was generated from the crystal structure of the nucleosome (13), with a CTF function and missing wedge applied (7). PCA classification was performed after the alignment and class averages were analyzed for resulting structural elements. The use of the template introduces a significant bias to the shape of the central density. However, our interest is the arrangement of specific dependencies surrounding this density, which are independent of the template used.

1. Langmore JP, Schutt C (1980) The higher order structure of chicken erythrocyte chromosomes in vivo. *Nature* 288:620–622.
2. Woodcock CL (1994) Chromatin fibers observed in-situ in frozen-hydrated sections—native fiber diameter is not correlated with nucleosome repeat length. *J Cell Biol* 125:11–19.
3. Zheng SQ, et al. (2007) UCSF tomography: An integrated software suite for real-time electron microscopic tomographic data collection, alignment, and reconstruction. *J Struct Biol* 157:138–147.
4. Castano-Diez D, Scheffer M, Al-Amoudi A, Frangakis AS (2010) Alignator: A GPU powered software package for robust fiducial-less alignment of cryo tilt-series. *J Struct Biol* 170:117–126.
5. Frangakis AS, et al. (2002) Identification of macromolecular complexes in cryoelectron tomograms of phantom cells. *Proc Natl Acad Sci USA* 99:14153–14158.
6. Egelman EH (2007) The iterative helical real space reconstruction method: surmounting the problems posed by real polymers. *J Struct Biol* 157:83–94.
7. Forster F, Pruggnaller S, Seybert A, Frangakis AS (2008) Classification of cryo-electron sub-tomograms using constrained correlation. *J Struct Biol* 161:276–286.
8. Yu Z, Frangakis AS (2011) Classification of electron sub-tomograms with neural networks and its application to template-matching. *J Struct Biol* 174:494–504.
9. Pierson J, Ziese U, Sani M, Peters PJ (2011) Exploring vitreous cryo-section-induced compression at the macromolecular level using electron cryo-tomography; 80S yeast ribosomes appear unaffected. *J Struct Biol* 173:345–349.

10. Schalch T, Duda S, Sargent DF, Richmond TJ (2005) X-ray structure of a tetranucleosome and its implications for the chromatin fibre. *Nature* 436:138–141.
11. Bednar J, et al. (1998) Nucleosomes, linker DNA, and linker histone form a unique structural motif that directs the higher-order folding and compaction of chromatin. *Proc Natl Acad Sci USA* 95:14173–14178.
12. Volkman N (2002) A novel three-dimensional variant of the watershed transform for segmentation of electron density maps. *J Struct Biol* 138:123–129.
13. White CL, Suto RK, Luger K (2001) Structure of the yeast nucleosome core particle reveals fundamental changes in internucleosome interactions. *EMBO J* 20:5207–5218.

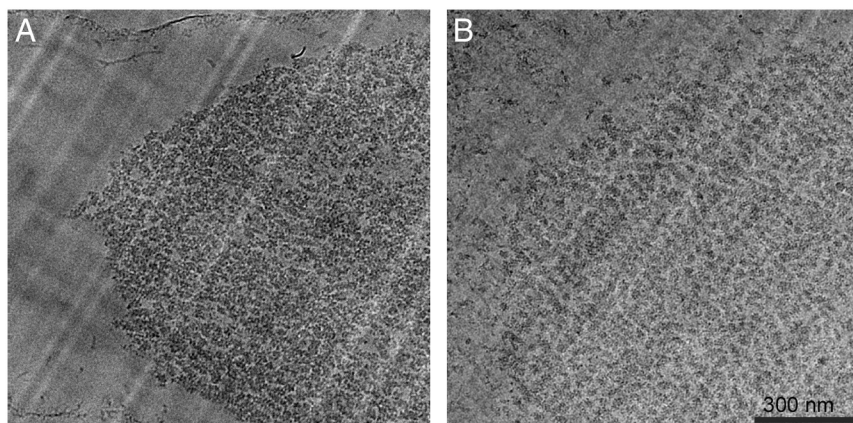


Fig. S1. Comparison of freezing conditions for chicken erythrocyte nuclei showing the osmotic effect in relation to ionic concentration. (A) Vitreous sections of nuclei high-pressure frozen in MLB buffer containing 2 mM $MgCl_2$ and 20% 1.5 kDa dextran. This dextran has no osmotic effect and thus does not have an effect on chromatin compaction (1). Distinct compact 30-nm fibers may be seen, but the sections are prone to fracture formation due to the type of dextran used, which prevents 3D structural analysis. (B) Vitreous sections of nuclei high-pressure frozen in buffer containing 20 mM NaCl and 20% 40 kDa dextran. The osmotic effect of this particular dextran maintains fiber compaction that is equivalent to that of 2 mM $MgCl_2$ ionic strength (compare A and B) and provides substantially better section quality, allowing us to use the data for 3D analysis. Many longitudinal fibers are present, but due to the nature of the contrast in the samples, top views are much more obvious than longitudinal views.

- 1 Eltsov M, Maclellan KM, Maeshima K, Frangakis AS, Dubochet J (2008) Analysis of cryo-electron microscopy images does not support the existence of 30-nm chromatin fibers in mitotic chromosomes in situ. *Proc Natl Acad Sci USA* 105:19732–19737.

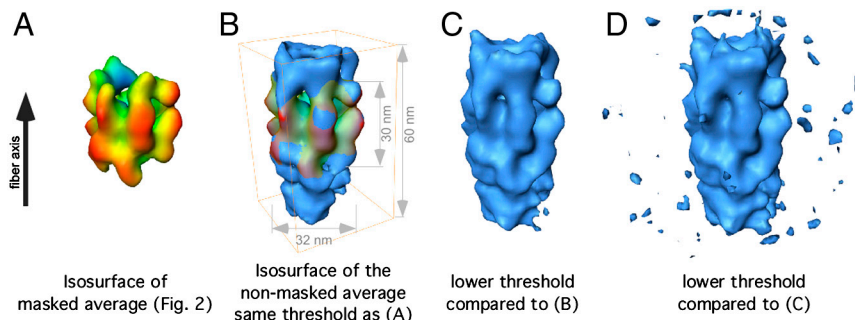
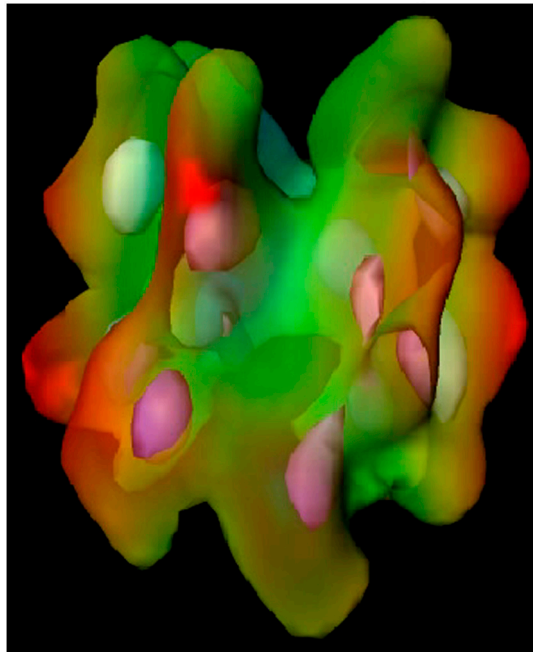
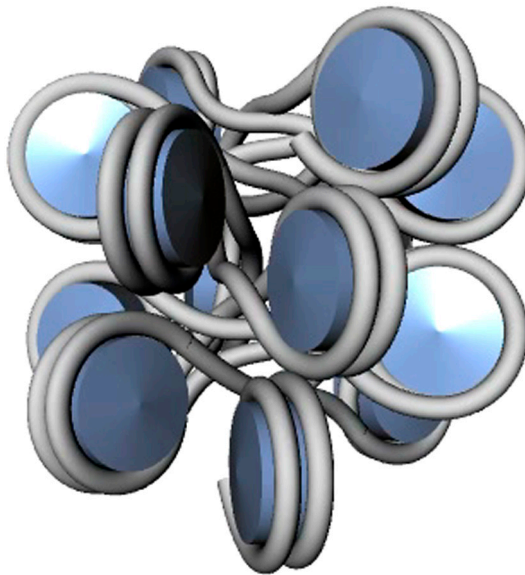


Fig. S2. Subtomogram average contoured at various thresholds. (A) Isosurface as presented in Fig. 2. The isosurface is masked to two gyres for visualization purposes. (B) Superposition of the masked (radial colors) and nonmasked subtomogram average (in blue) rendered at identical thresholds. The nonmasked subtomogram average is approximately 60 nm long and shows significant densities outside the mask used for subtomogram averaging. The densities outside the mask are largely unstructured because they were not considered in the averaging procedure. (C and D) Isosurface visualization of the subtomogram average at a lower threshold compared to B. No additional densities, other than those resulting from noise, appear in the surrounding of the fiber indicating that very few (if any) misaligned fibers contribute to the average. The densities outside the mask used for subtomogram averaging have a cone shape as a consequence of the slight flexibility of the averaged fibers.



Movie S1. The rotating subtomogram average. A rotating isosurface representation of the subtomogram average, which is pseudocolored according to the cylindrical radius. Higher threshold densities are shown in white-blue, indicating that the fiber has a two-start geometry.

[Movie S1 \(MOV\)](#)



Movie S2. The fiber model after fitting the nucleosomes in the density map. The nucleosomes are placed at the positions of the correlation peaks shown in Fig. 3B, which are visualized in blue. The suggested path of the linker DNA that is assumed to cross the fiber axis is modeled in gray.

[Movie S2 \(MOV\)](#)

